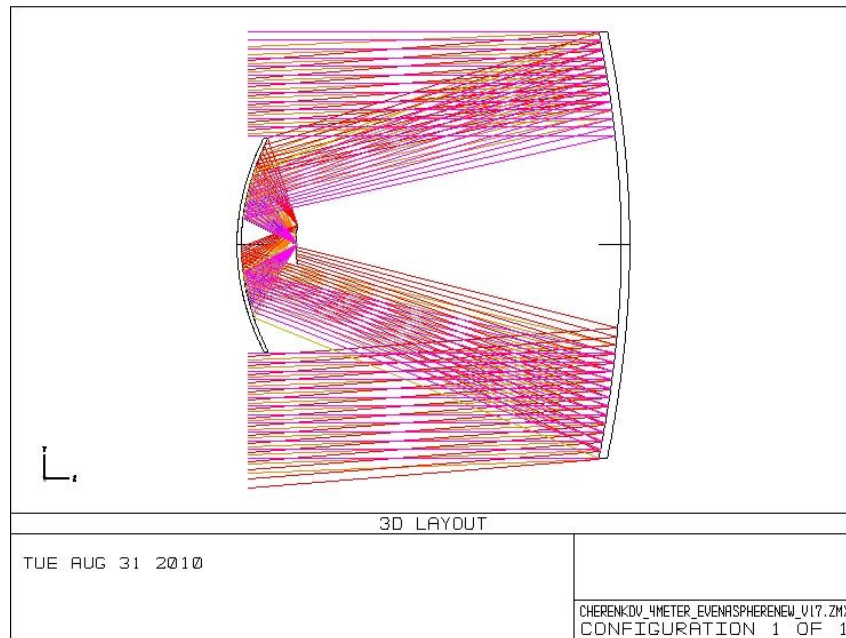


# A study of the optics of a 4m dual mirror SST

Version 1.0, 2011-03-09

Jürgen Schmoll, CfAI Netpark, Durham University



## 1 Introduction

This document describes the further development of the aplanatic two-mirror design approach discussed on the CTA UK meeting in Liverpool on Jan 29<sup>th</sup>, 2010. The current design is referred to V17 as it is the product of an on-going design iteration to curtail it to the SST requirements.

## 2 Optical design

The focal length is 2283 mm, providing a plate scale of 39.6 mm/°.

The focal ratio is  $f/0.57$ .

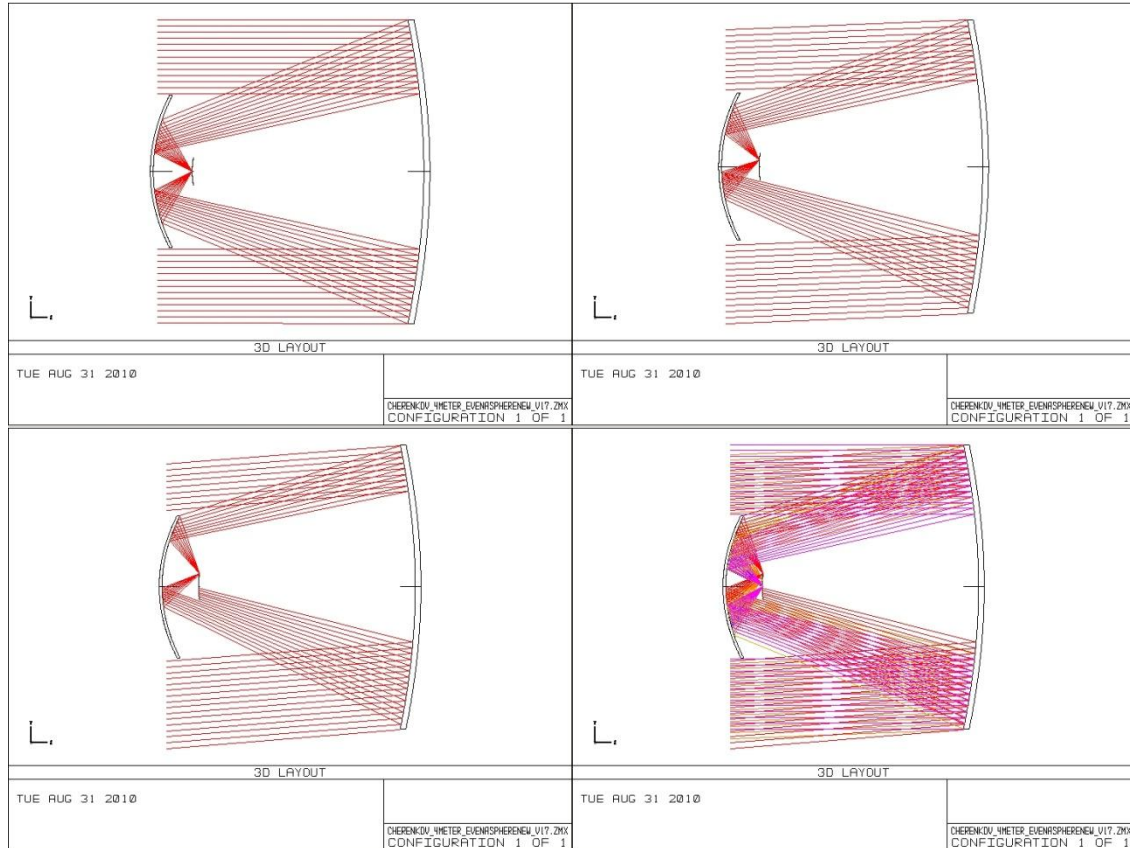


**Figure 1: Layout of the current design. Field angles 0°, 2°.25, 4.5° and all angles.**

Element	Diameter	R.O.C.	Shape	Dist to ...
M1 (primary)	4000 mm	-	Even Asphere	... M2: 3561.1mm
M2 (secondary)	2002mm	-	Even Asphere	... detector: 510.7 mm
Detector area	362 mm	1000 mm	Spherical	-

**Table 1: Element properties.**

### 3 Optical element description

As before, the pure polynomial description has been used for M1 and M2:

$$x = \alpha_1 r^2 + \alpha_2 r^4 + \alpha_3 r^6 + \alpha_4 r^8 + \alpha_5 r^{10} + \alpha_6 r^{12} + \alpha_7 r^{14} + \alpha_8 r^{16}$$

Table 2 lists the coefficients of M1 and M2.

Mirror	M1	M2
$\alpha_1$	-5.4280255e-005	0.0002435033
$\alpha_2$	-3.3912879e-013	3.8794144e-011
$\alpha_3$	1.3451359e-018	-1.3111154e-016
$\alpha_4$	-1.2900035e-024	2.8830939e-022
$\alpha_5$	6.8508142e-031	-3.9781971e-028
$\alpha_6$	-2.0059722e-037	3.3371289e-034
$\alpha_7$	3.0563336e-044	-1.542123e-040
$\alpha_8$	-1.8853301e-051	2.987865e-047

**Table 2: Even asphere coefficients for mirrors M1 and M2.**

Note: As the use of tessellated surfaces in ZEMAX is very cumbersome, the mirrors have been modelled as monolithic surfaces, with separate surfaces acting as central obscurations to model the vignetting characteristics. As tessellation allows further design freedom by the introduction of steps between adjacent panels [1], on a later stage it may be worthwhile to study if a tessellated design will improve image quality. However the introduction of tessellation steps will impair the isochronous character of the current design.

# 4 Vignetting and geometrical throughput

The overall geometrical throughput is 75% on axis and 71% at the field edge at 4°.5. The effective collecting area varies between 9.4 m<sup>2</sup> on axis and 8.9 m<sup>2</sup> at the field edge.

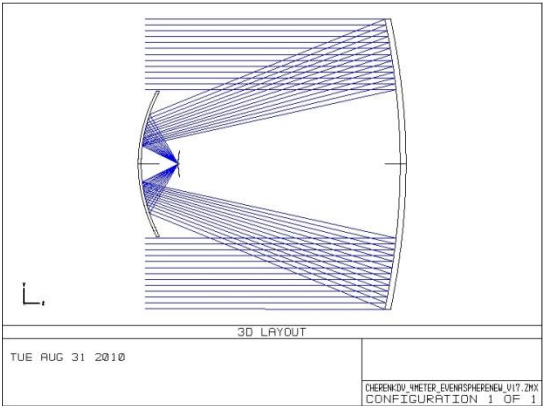


Figure 2: Layouts with paraxial beams.

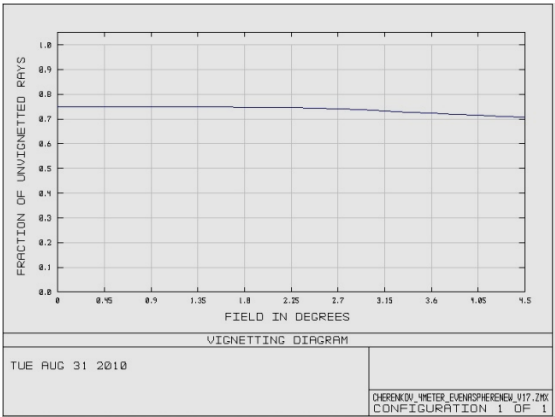


Figure 3: Total geometrical throughput of the current design plotted versus field angle.

Fig. 4 shows the effect of both obscurations for different field angles, using the spot diagrams in the focal plane as directional cosines. As both obscurations are not at the pupil, the varying of the obscuration effect with the field angle cannot be avoided.

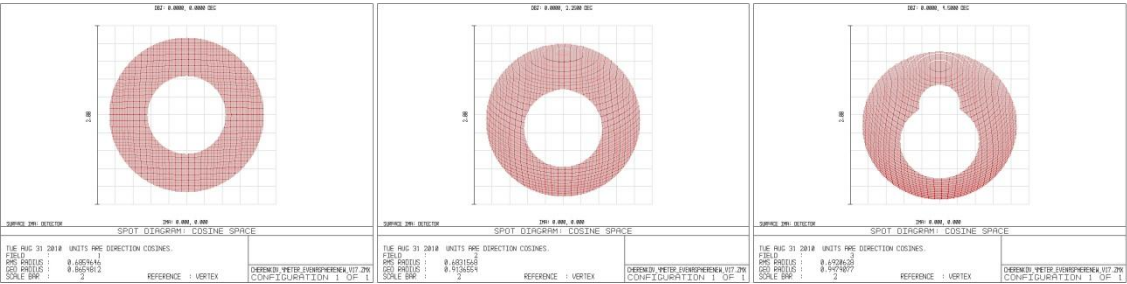
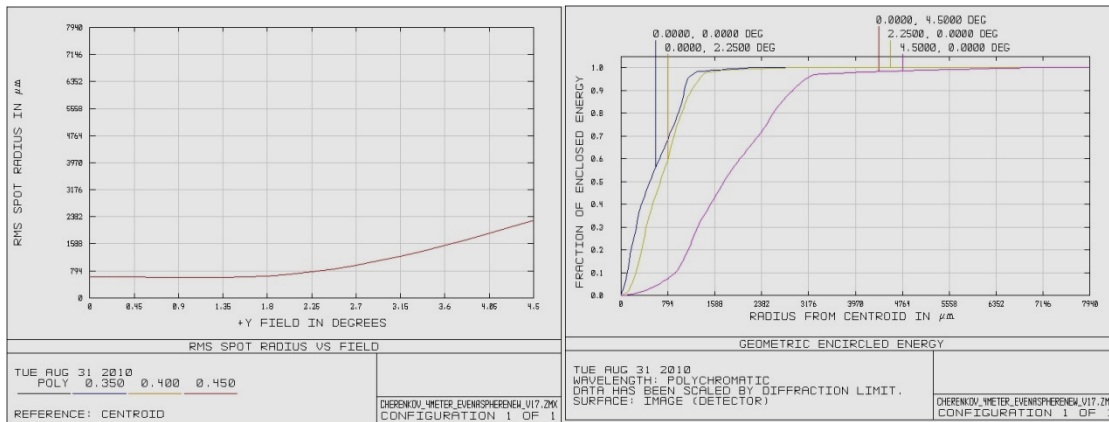


Figure 4: Vignetting pattern in the focal plane depending on the field angle ( 0°, 2°.25 and 4°.5)

## 5 Image quality

Due to the higher weights on larger field angles, the rms spot radius is varying less with field angle, and the maximum value is below 2.4mm – so the rms spot size does not exceed 4.8mm or  $0''.12$  (7.3 arc min) on the sky. As fig. 6 shows,  $EE_{80}$  is reached within a 5mm spot diameter for all field angles.



**Figure 5: RMS spot size vs. field (left) and EE of different field points within  $0''.2$  around the centroid (right).**

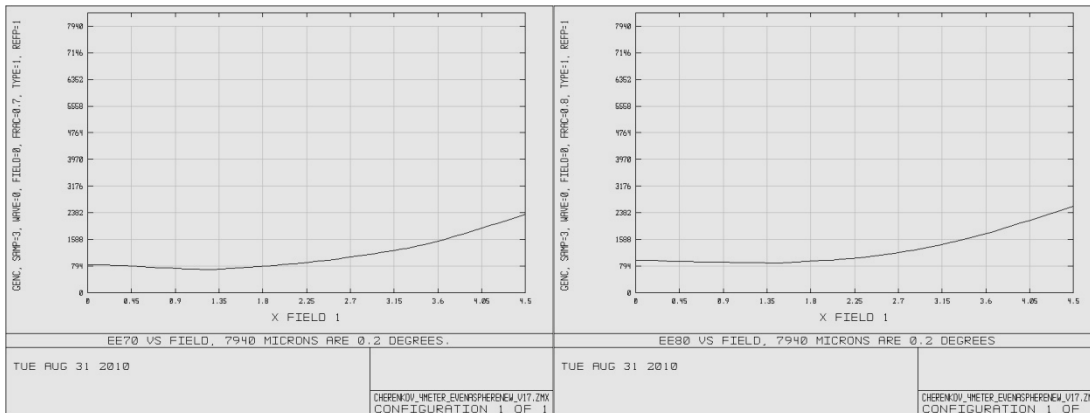


**Figure 6:  $EE_{70}$  (left) and  $EE_{80}$  (right) versus field angle, the 7940 μm representing the  $0''.2$  limit.**

The resolving power has been simulated by geometric image analysis of two point sources in  $0''.5$  (fig. 7) and  $0''.2$  (fig. 8) separation of each other. The simulation shows that these sources are resolved at all field angles up to  $4''.5$ .

When simulating the situation of two point sources separated by  $0''.2$  sampled by pixels of 6.5mm size, it becomes clear that the resolution is rather limited by the pixel size instead of the optics (fig. 9).

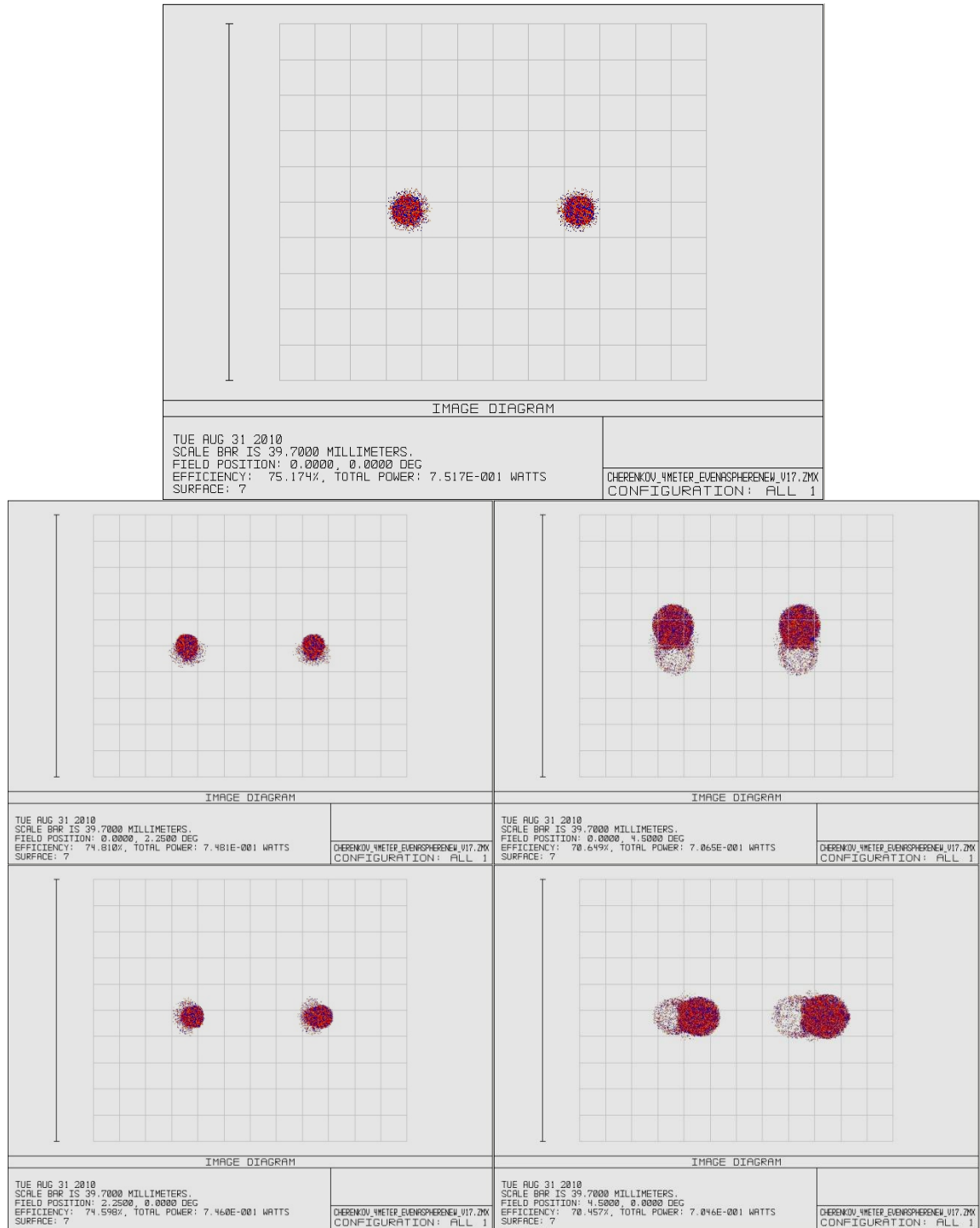


**Figure 7: Image simulation of two point sources of 30' separation. Top: Paraxial, centre field angles (0°/2°.25) and (0°/4°.5), bottom field angles (2°.25/0°) and (4°.5/0°).**

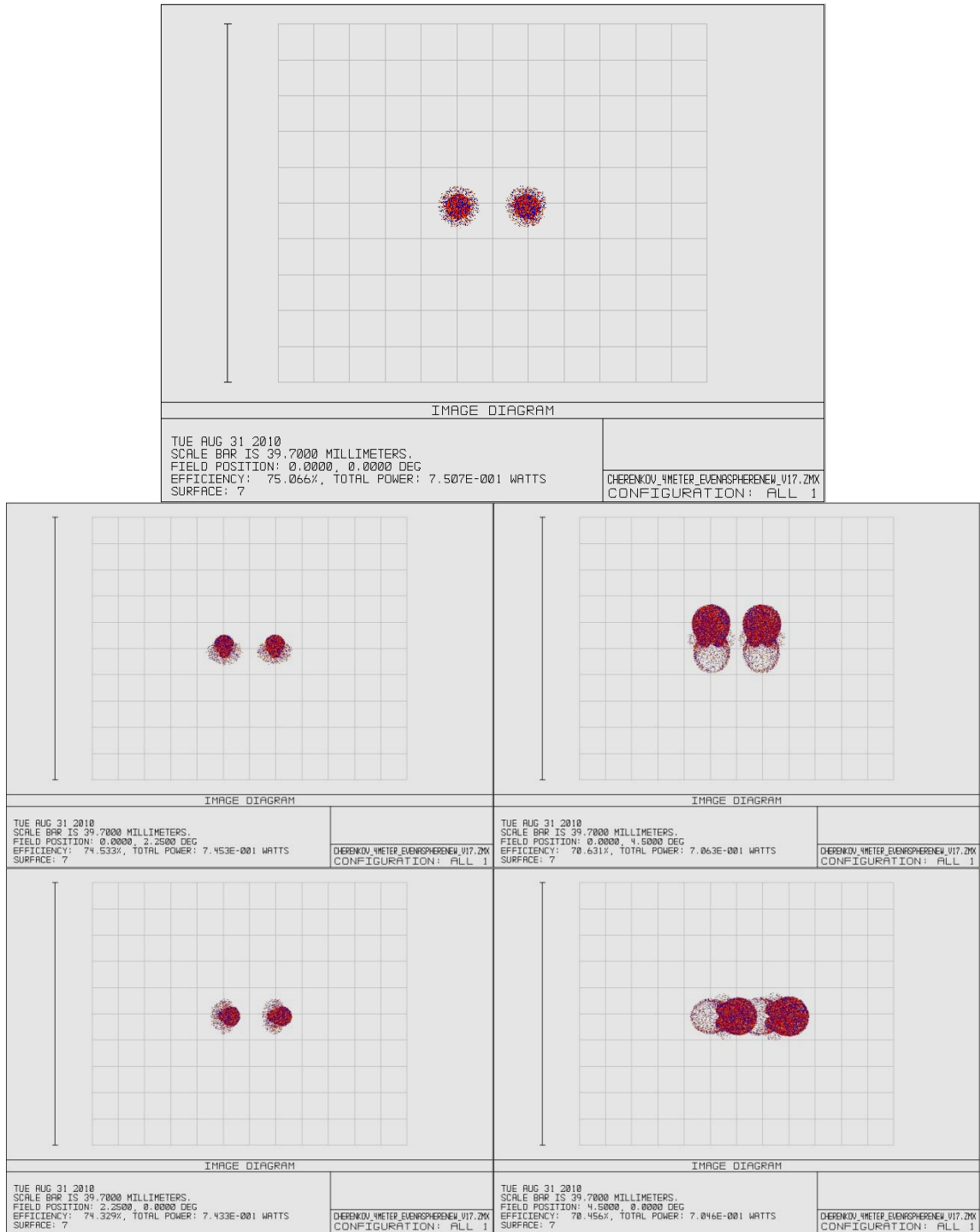


**Figure 8: Image simulation of two point sources of 12' separation. Top: Paraxial, centre field angles (0°/2°.25) and (0°/4°.5), bottom field angles (2°.25/0°) and (4°.5/0°).**

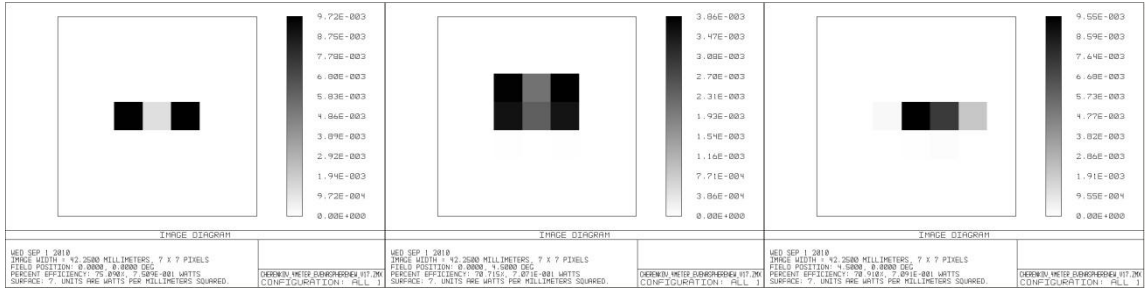


**Figure 9: Image simulation of the situation in fig. 8, assuming 6.5mm square detector pixels.**  
**From left to right: On axis, at (0°/4°5) and at (4°/5°0).**

The distortion is of the barrel type and reaches 2.5% at maximum field angle (fig. 10).

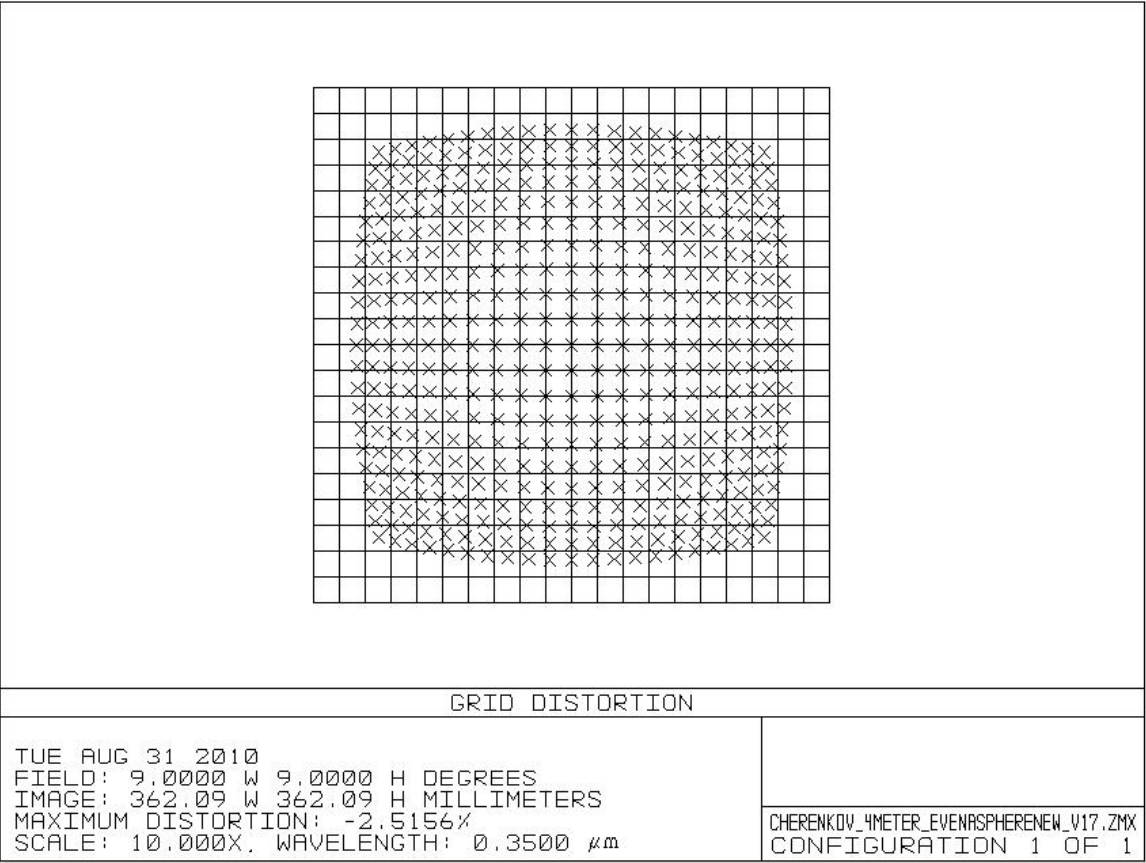


**Figure 10: 10x exaggerated distortion diagram over the full field of 9° x 9°.**



## 6 Detector incidence angles

ZEMAX shows the maximum angle the rays hit the focal plane as geometric radius when the spots are plotted as directional cosines. As fig. 14 shows, the maximum cosines vary between the field positions (0/0) and (0/4.5) as indicated in table 3. The cosine ZEMAX displays is the angle between the flat focal plane (means the plane orthogonal to the optical axis) and the incoming beam, see  $\theta$  in figure 13. With the auxiliary angles

$$\varphi = 90^\circ - \theta$$

and

$$\beta = \arcsin \frac{R}{r}$$

with  $R$  as distance of the chief ray from the optical axis and  $r$  the detector plane curvature. The real maximum angle at a curved detector plane is determined by

$$\delta = \varphi - \beta$$

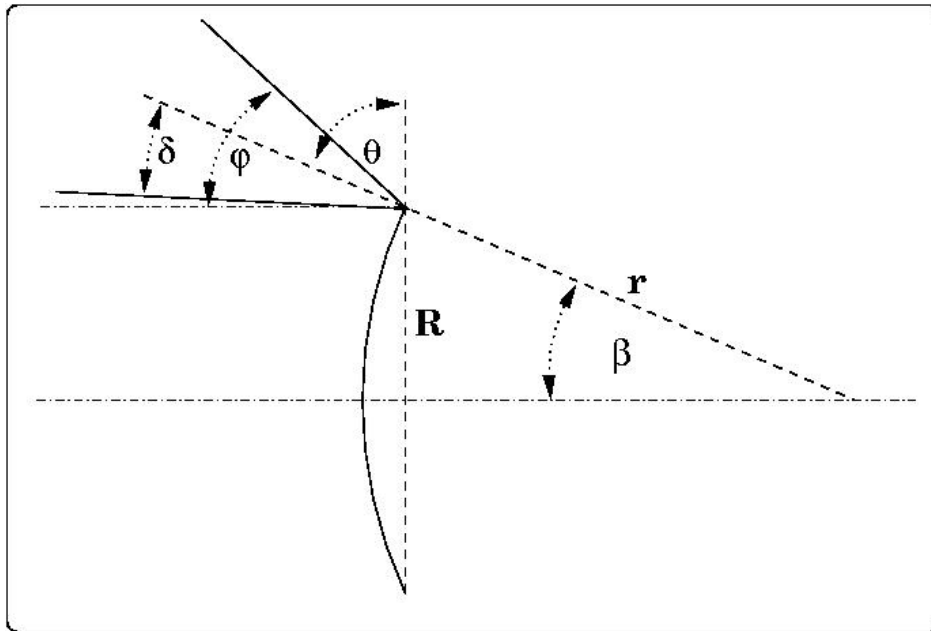


**Figure 11: Angles involved in the detector angle determination.**  
 **$R$  is the geometric radius of the focal plane.  $r$  is the focal plane radius of curvature.**

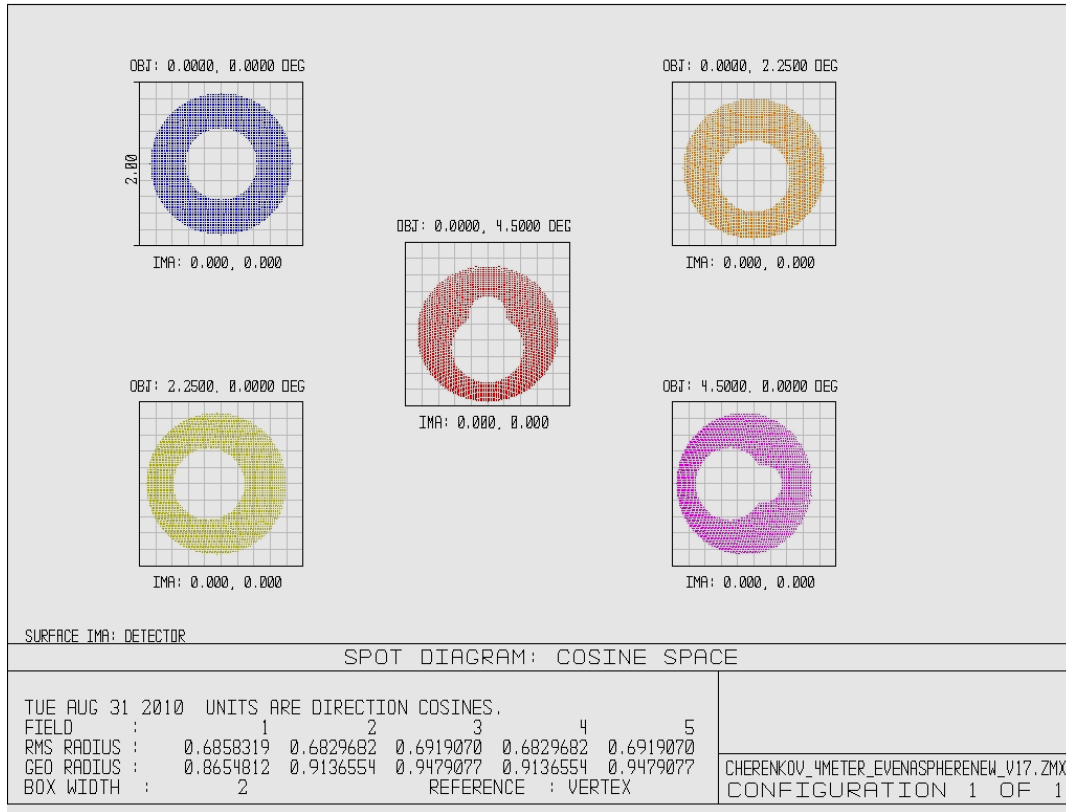


**Figure 12: V17 directional cosines for different field angles.**

Version	Field point	cos $\theta$	$\phi$ [°]	$\beta$ [°]	$\delta$ [°]
V17	(0/0)	0.8655	59.9	0	59.9
	(0/4.5)	0.9479	71.4	10.4	60.0

**Table 3: Angles of incidence of the current design.**

Table 3 summarises the angles on axis and at the maximum field angles. The angles on the detector are not exceeding 60°. The difference of the maximum field angles between the field centre and the field edge is with 0°.1 negligible. While the detectors have to cope with incidence angles of up to 60°, there is no significant signal nonuniformity introduced as the maximum incidence angle varies so little.

## 7 Tolerancing

The tolerancing was undertaken in two steps:

1. Standard tolerancing, treating optics monolithically
2. Boresight analysis to evaluate effect of panel misalignment

### 7.1 Standard tolerancing

At this stage the influence of tilts, decentres and surface deviations on the point spread function is investigated. Table 4 shows the magnitude of deviations applied and adjusted to assure that the total increase of the rms spot sizes does not exceed 10%.

As tolerances of polynomial coefficients cannot be easily varied using ZEMAX, the approximate radii of the surfaces were added to the polynomial description again, assuring the overall shape remained unchanged by just varying the coefficients of the surface where the radius was added and watching the system behaviour. The assumed radii were 8 m for M 1 and 2.4 m for M2.

The surface irregularity was modelled using the ZEMAX parameter TEZI which is based on the Zernike surface model. All 231 Zernike terms available have been used to assure that not only bumps of low spatial frequency but also ripples are considered as they may be introduced by the mirror manufacturing process. As the small scale structures deviations are smaller in size, the deviations for Zernike coefficients between 2 and 21 (“*surface waviness*”) have been modelled with 20  $\mu\text{m}$  rms (M1) and 50  $\mu\text{m}$  rms (M2). The higher zernike terms between 22 and 231 (“*surface irregularity*”) have been considered of 1  $\mu\text{m}$  rms.

***Note not to confuse “surface irregularity” with surface roughness that addresses the much finer structure of an optical surface that gives rise to scattering. Scattering has to be dealt with in a different way and as it strongly depends on the mirror manufacture method chosen, it has not been modelled yet.***

The only compensator allowed to counteract the effects of tolerances was the focus, namely the distance between M2 and the detector array. The focus changed  $\pm 3.74$  mm around the design position.

The nominal rms spot radius changed from 1.53 mm to 1.67 mm, which is a deterioration of 9.2 %. Worst offenders are the large scale surface waviness and the tilt of M1.

After the tolerance sensitivity analysis, a Monte Carlo simulation of 8000 cases has been undertaken to see how the system is likely to behave under a normal distribution of tolerances. As ZEMAX cannot perform the Zernike evaluation in this mode, the TEZI operands had to be removed so the surface shape error is not included. In this run, the nominal spot radius changed from 1.53 mm to 1.66 mm (8.5% increase), so 1% less as if the Zernike deviations were included.

The Monte Carlo analysis revealed:

Worst case: 1.92 mm spot radius (26% increase)

Mean: 1.59 mm (4.3% increase)

98% of all cases within 1.71 mm (12.2% increase)

90% of all cases within 1.66 mm (8.4% increase)

Error	Surface	Tolerance
Distance deviation	M1 to M2	+/- 5 mm
	M2 to detector array	(+/- 5 mm) (*)
Surface waviness	M1	20 $\mu\text{m}$ rms
	M2	50 $\mu\text{m}$ rms
Surface irregularity	M1	1 $\mu\text{m}$ rms
	M2	1 $\mu\text{m}$ rms
Radius deviation	M1	+/- 10 mm
	M2	+/- 3 mm
	detector array	+/- 3 mm
Element decenter	M1	+/- 5 mm
	M2	+/- 5 mm
	detector array	+/- 5 mm
Element tilt	M1	+/- 0.14°
	M2	+/- 0.14°
	detector array	+/- 0.14°

**Table 4: Tolerances during the standard tolerancing process.**

(\*) Caveat: The M2 to detector array distance tolerance is of no practical value as it is directly eradicated by the focus compensator ! See also discussion of defocuses caused by flat detector tiles and depth of field effects, chapters 9 and 10.

## 7.2 Boresight analysis

The reason for the boresight analysis is to get an idea of the tolerable amount of residual misalignment of different panels with respect to each other. While the former tolerancing assumed monolithic optics, now a pure tilt and decenter analysis was performed to observe the shift of the image by panel misalignment.

The maximum perturbation chosen was a total misalignment within half a pixel of 6.5mm size. As for different panels the direction of misalignment may change, the boresight error was restricted to 1/3 of a pixel to allow for some statistical distribution of misalignments. Hence, element tilts and decenters have been reduced until the boresight error was below 2.15mm.

Table 5 shows the values derived for M1 and M2. Albeit the whole element has been shifted, this result shows what would happen if parts of a mirror would move with respect to others. So the values of misalignment should be interpreted as deviations of different panels from each other, in contrast to the values of table 4 which address the whole mirror.

Element decenter	M1	$\pm 2 \text{ mm}$
	M2	$\pm 2 \text{ mm}$
Element tilt	M1	$\pm 1'$
	M2	$\pm 3'$
	Focal plane	$\pm 5'$

**Table 5: Tolerances during the boresight analysis.**

A Monte Carlo analysis has been performed as well with 8000 cases.

Worst case: 2.4mm error (37% of one pixel)

Mean: 0.85mm (13% of one pixel)

98% within 1.85mm (28% of one pixel)

90% within 1.44mm (22% of one pixel)

## 8 Possible improvements

An improvement can be undertaken by introducing tessellation steps as this measure allows more degrees of freedom with respect to the optical design. The caveat is a potential loss of the isochronous character of the current design that can be realized tessellated but incorporates no steps.

There is a minor improvement possible by introduction of a conic constant to the detector plane, however this constant (about 4.8 to 5) only introduces marginal improvement on the possible cost of a more complicated manufacture of the detector positioning system.

## 9 Impact of flat detector tiles on defocus

While the detector focal plane has a convex curvature of 1000mm, the detectors in question are flat. While microchannel plate substrates may be slumped to a required curvature before etching the channels, other detector types that are e.g. based on Silicone do not have this capability. As in the tolerancing runs the distance tolerance of M2 to the detector plane is directly undone by the defocus compensator, the given tolerance of  $\pm 5\text{mm}$  has no practical value. With a focal ratio of  $f/0.578$ , each defocus will cause an image broadening of  $1/0.578 = 1.73$  times the defocus distance.

Using the example of an 8x8 PMT array of 52 mm side length, the impact of the flat detector substrate on the image quality has been calculated.

With  $R$  as the maximum distance of a curved surface from the optical axis and  $r$  as the curvature radius of the surface, the sag  $s$  can be calculated as

$$s = r - \sqrt{r^2 - R^2}$$

The total sag of the focal plane for example ( $R=181\text{mm}$ ,  $r=1000\text{mm}$ ) is  $s = 16.517\text{mm}$ .

The same equation can be used to calculate the total deviation of the curved focal plane from a flat piece which centre is aligned orthogonally to the vertex of the focal plane at the tangent point.

For the PMT array, the largest distance from the centre is  $R=36.8\text{mm}$ . The defocus in the corners of the square array calculates to  $0.68\text{ mm}$ , giving rise to an image broadening of  $1.18\text{ mm}$  in diameter or  $18\%$  of the pixel size.

This defocus is variable over the field of view, disappearing at each tile centre and being at maximum at the tile corners unless each tile is aligned to have the smallest spots in an annular zone around the centre.

If this error is tolerable, needs to be decided by taking into account other deviations as caused by the structure of the  $\gamma$ -ray shower. Apart from the intrinsic shower width, depth of field effects will introduce defocus inevitably.

The ZEMAX simulation by imaging a 5x5 spot array onto one tile shows no significant difference between curved and flat surfaces. This can be explained with the focus being in a type of a line (as in spherical aberration).

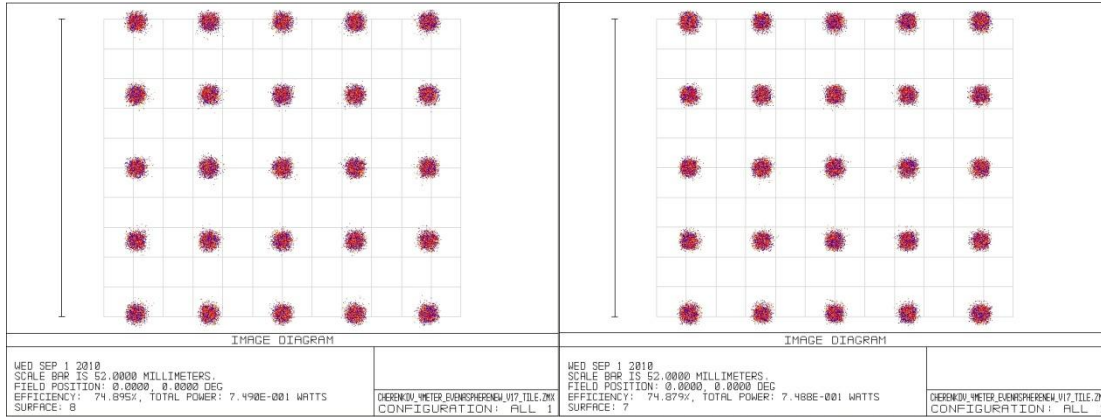


**Figure 13: Effect of flat tiling of the curved focal plane. Over one 52mm side length square sensor tile, the spot images change not significantly when the detector surface is not curved. Left shows curved, right flat image of 52mm side length (see also scale bar).**

## 10 Impact of depth of field effects of $\gamma$ -ray showers

The nominal design distance assumes the conjugate imaging of an object in 10km distance to the focal plane. However, this distance is just the order of magnitude for average  $\gamma$ -ray showers. In fact, this distance will vary caused by

1. The energy of the shower (higher energetic showers appear in lower parts of the atmosphere.
2. The zenith distance  $\vartheta$  of the area the telescope is pointing at magnifies the true shower height over ground by the factor  $\frac{1}{\cos \vartheta}$ .
3. The extension of the Cherenkov shower structure itself.

The image distance  $d_i$  depends from the object distance  $d_o$  as described by the Gaussian imaging equation:

$$\frac{1}{f} = \frac{1}{d_i} + \frac{1}{d_o} \Rightarrow d_i = \left[ \frac{1}{f} - \frac{1}{d_o} \right]^{-1}$$

For  $d_o = \infty$  follows  $d_i = f = 2283$  mm.

For  $d_o = 10\text{km}$  follows  $d_i = 2283.52$  mm, the image forms 0.52mm behind the infinity focus. In the worst case, assuming the bottom end of a high energy shower at a distance of  $d_o = 5\text{km}$ ,  $d_i$  becomes 2284.04 mm.

The difference between the infinity and the 5km object distance image in the focal plane is 1.04 mm. As the system is focused at 10km, the distances of different object heights are  $\pm 0.52\text{mm}$ . Due to the  $f/0.578$  system this causes a blur of up to 0.9mm or 14% of a pixel.

While an elevation-dependent refocusing may be introduced to compensate for the defocus caused by the varying zenith distance, the other depth of field effects cannot be compensated. Any sort of “auto-focus” system is not feasible, taking the short duration of the shower events into account.

The effect of the varying object distance on the encircled energy is shown in figure 14. There is no significant effect on the encircled energy when varying the object distance between 5km and infinity without refocusing the system.

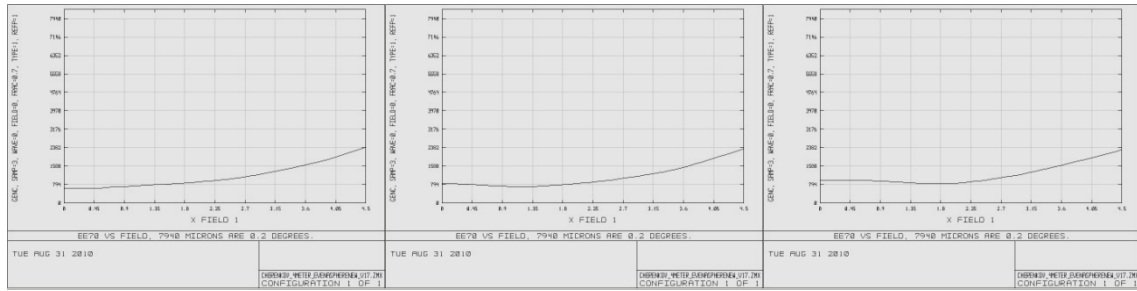


Figure 14:  $EE_{70}$  versus field for object heights of 5km (left), 10km (centre) and infinity (right).

## 11 Plate scale and telescope scaling

In the discussion about the plate scale that lead to the redesign of former versions towards the current one, the option of downscaling the telescope has been discussed. To do this, the effective focal length must be brought down from 2283mm to 2005mm while the linear shrinkage of the mirrors would reveal a telescope with 88% of the current size and 77% of the current light collection area. The primary diameter comes down to 3.5m, the secondary to 1.76 and the light collection area varies between  $7.25\text{m}^2$  on axis (from  $9.4\text{m}^2$ ) and  $6.86\text{m}^2$  at the field edge (from  $8.9\text{m}^2$ ).

A test had been performed, indicating that such a modification is feasible with similar or slightly smaller spot diameters, even when keeping the focal plane curvature at 1000mm to allow the detector installation. The distances and even polynomial surface coefficients change to adapt to the new design.



## 12 Alignment of the segmented telescope

The alignment of the telescope incorporates the following steps:

1. Co-alignment of the (assumed) six segments that make up M1.
2. Alignment of the (assumed) monolithic M2.
3. Adjustment of the detector tiles to fit the curved focal plane.
4. Adjustment of the whole detector plane with respect to the telescope.

A new ZEMAX model has been created with six configurations. A user-defined aperture was created in the shape of a 60-degree semicircle. In each of the configurations this semicircle was rotated by 60 degrees so that the primary was effectively split up into six radial parts. Using coordinate breaks for M1, M2 and the focal plane, the effects of translational and angular misalignment have been simulated.

### 12.1 Co-alignment of the primary mirror segments

For this step, a distant light source is necessary. For the ZEMAX model an artificial light source of 2 arc seconds angular extension was assumed in a distance of 10 kilometers. This means a linear extension of the source of 0.1m, realized for example by a reflector light or an LED array on a tall mast.

The concept is to point the telescope structure to the horizon to install the M1 panels in vertical position. Then the focal point of M1 is used to co-align the segments. This focal point is located 1.3m further away from M1 than the M2 vertex. A flat screen has to be installed on the optical axis to assist during this alignment stage.

As M1 is not parabolic and the actual shape optimised together with M2, the focal point is highly aberrated. However, there is a strong maximum in the centre and a well defined annulus at the edge that can assist in the alignment process.

The following images show the effects of tilts, translational displacements and defocus of one of the six segments with respect to the others that are in perfect alignment. As fig. 15 shows, each single element gives rise to a wedge shaped appearance while the combination of all segments creates the aberrated, rotationally symmetrical spot image.



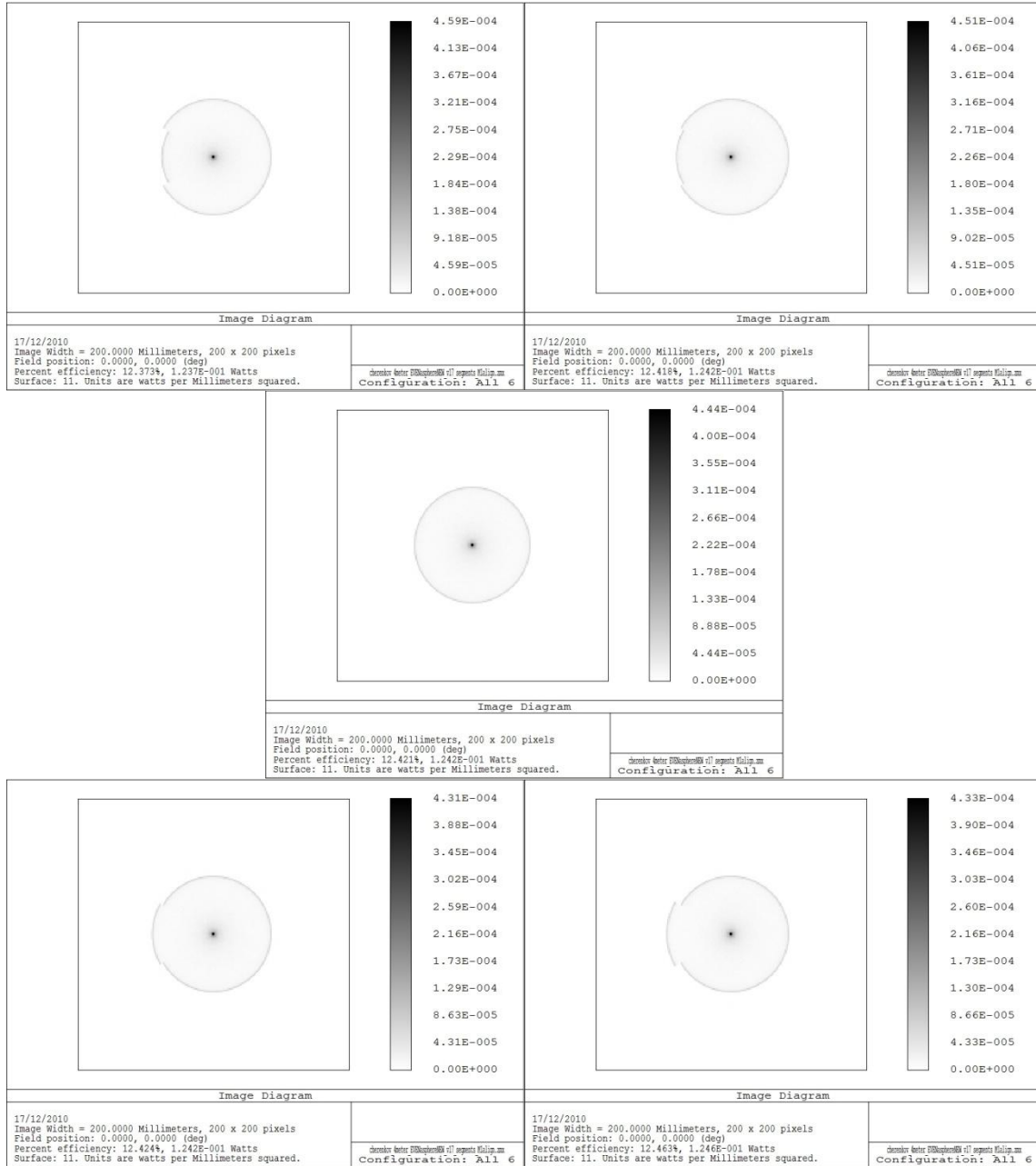


**Figure18: Defocus of one element with respect to the others. Top row -20mm, -10mm. Centre defocus 0mm (element in focus with the others), bottom defocus +10mm, +20mm.**

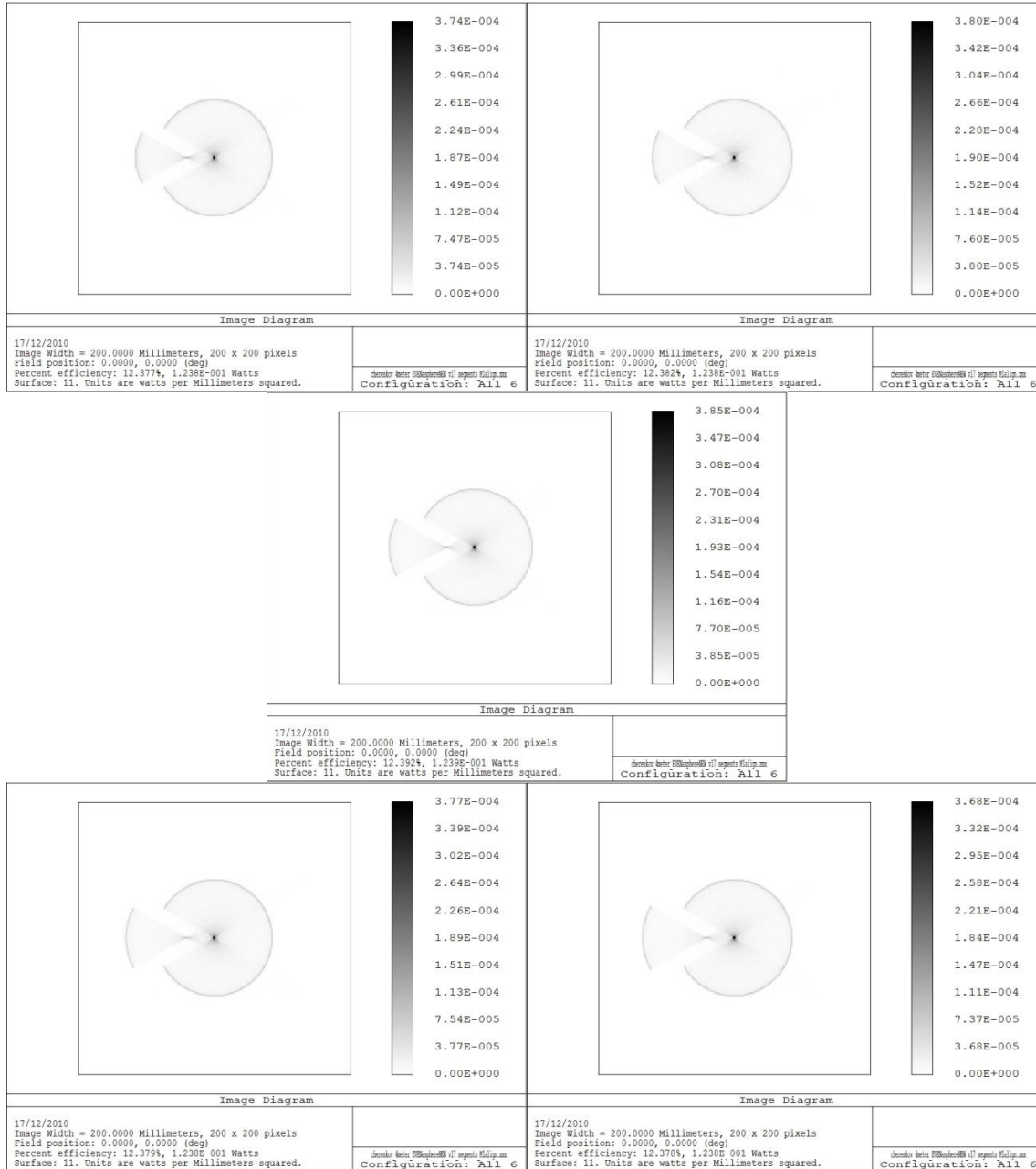


**Figure 19:** Same sequence as in fig. 18 but element offset by 20mm in x to show the image change to the defocused segment. From top to bottom, left to right defocus of -20mm, -10mm, 0, 10mm, 20mm.

The simulations show that defocus can be detected as a scale change of the wedge pattern formed at the auxiliary screen. The focus test is most sensitive when the tilts and decenters are aligned as the defocus reveals a discontinuity of the circumference of the large halo.

The difficult part is to distinguish between tilt and offset as the result is similar, shown by figures 16 and 17. An alternative method has to be used to decouple both effects to make them adjustable on their own. Possible solutions are

- the use of a laser pointing to a particular part of each segment that is well defined in x/y. This may be a tiny datum surface at the edge. This allows to align the tilts out. Then each misalignment showing up as image translation in the intermediate focus can be cured by translation of the segment in question.
- the use of datum surfaces on the sides of each mirror to rule out any translational misalignment. Even a laser tracker target could be installed on the edge of each segment, allowing it to be moved into the correct translational position. Then, each misalignment observed at the intermediate focus is to be cured by tilt changes of the segment in x and y.

## **12.2 Adjustment of the secondary mirror**

M2 has to be installed centrally in front of M1 and in the correct focus. Once bolted into position, M2 has to be tip/tilt adjusted to allow a paraxial beam to hit the detector plane centrally.

Figures 20, 21 and 22 show the effect of the paraxial spot image for decenter, tilt and defocus of M2. Those images can be used as a guide line to get M2 aligned.



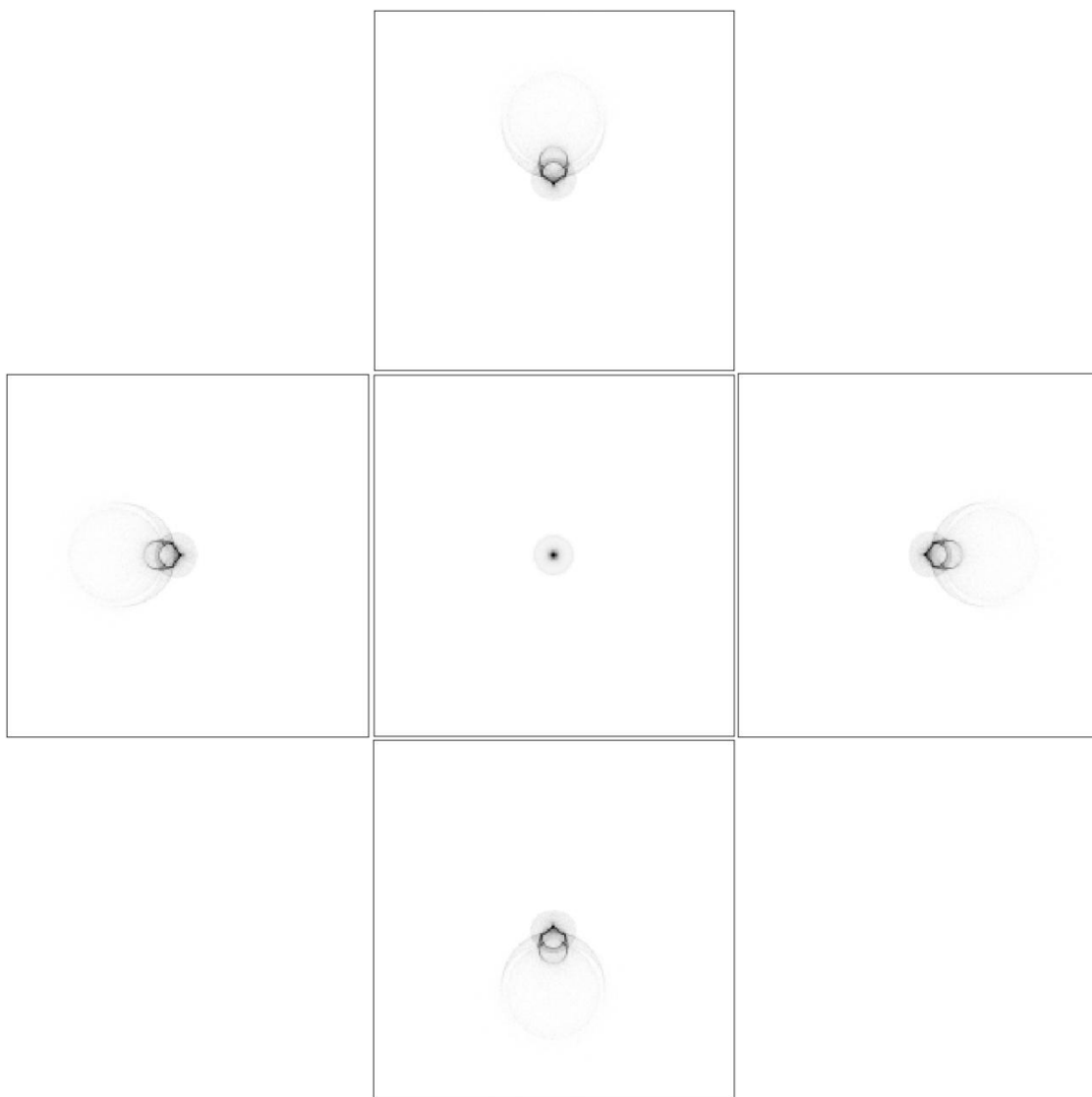


**Figure 21: Tilt of M2 about x (column) and about y (row) by  $-0.5^\circ$ ,  $0^\circ$ ,  $0.5^\circ$ . Box size again 20mm.**

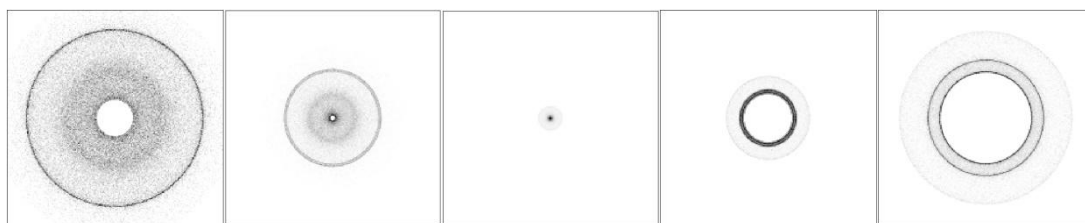


**Figure 22: Through-focus simulation:  
Additional distance M2 to M1 from left to right 5mm, 2.5mm, 0mm, -2.5mm, -5mm.**

### 12.3 Alignment of the detector tiles on the detector plate

This step can be performed in the laboratory by using a focusing light source on a curved rail system. The mobile light source focuses light onto the detector, and by putting a screen on each detector panel, the spot size can be minimised by tilting each detector tile accordingly.

### 12.4 Alignment of the detector plate inside the telescope

This can be done firstly by analysis of the paraxial light source (control of decenter and focus), followed by a laser either bounced off the detector plane (laser launched through a central hole of M2) or a laser bounced of M2 (laser launched at detector plane). Further fine tuning can be done by moving the telescope unit to different field points to observe the spot quality across the full field of view.

### 12.5 Fine tuning and in-operation analysis

There is the chance of occasional misalignment during operation, caused by long-time effects or episodes of stress (e.g. after a storm). The main rule is that each multiple image caused by a single object points to the M1 panel misalignment while global shape deviations point to the tilt/shift of M2 or the detector plane.

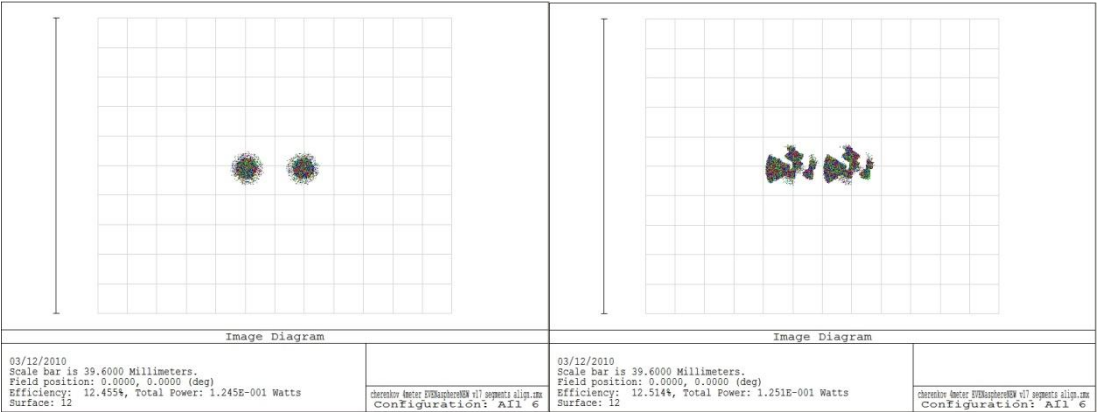


**Figure 23: Example of panel misalignment after stress. The perfect spot image of a double source (left) is distorted due to different tilts and shifts of the M1 panels.**



## **13 Literature**

- [1] **Schliesser, Mrizoyan 2008: Wide-field prime-focus Imaging Atmospheric Cherenkov Telescopes: A systematic study**
- [2] **Vassiliev, Fegan, Brousseau 2007: Wide field aplanatic two-mirror telescopes for ground based  $\gamma$ -ray astronomy**